Editors' Suggestion

Structural and optoelectronic properties of thin film $LaWN_3$

Rebecca W. Smaha,[1,*] John S. Mangum,[1] Ian A. Leahy,[1] Julian Calder,[1] Matthew P. Hautzinger,[1] Christopher P. Muzzillo,[1] Craig L. Perkins,[1] Kevin R. Talley,[1] Serena Eley,[2,3] Prashun Gorai,[1,4] Sage R. Bauers,[1] and Andriy Zakutayev[1,†]

[1]*National Renewable Energy Laboratory, Golden, Colorado 80401, USA*

[2]*Department of Physics, Colorado School of Mines, Golden, Colorado 80401, USA*

[3]*Department of Electrical & Computer Engineering, University of Washington, Seattle, Washington 98195, USA*

[4]*Department of Metallurgical and Materials Engineering, Colorado School of Mines, Golden, Colorado 80401, USA*

(Received 28 April 2023; accepted 28 July 2023; published 23 August 2023)

Nitride perovskites are an emerging class of materials that have been predicted to display a range of interesting physics and functional properties, but they are highly underexplored due to the difficulty of synthesizing oxygen-free nitrides. $LaWN_3$, recently reported as the first oxygen-free nitride perovskite, exhibited polar symmetry and a large piezoelectric coefficient. However, the predicted ferroelectric switching was hindered by a large leakage current, which motivates better understanding of the electronic structure and optical properties of this material. In this article, we study the structure and optoelectronic properties of thin film $LaWN_3$ in greater detail, employing combinatorial techniques to correlate these properties with cation stoichiometry. We report a two-step synthesis method that utilizes a more common radio frequency substrate bias instead of a nitrogen plasma source, yielding nanocrystalline films that are subsequently crystallized by *ex situ* annealing. We investigate the crystal structure and composition of the combinatorial films produced by this method, finding polycrystalline La-rich films and highly textured W-rich films. The measured optical absorption onset (2.5–3.5 eV) and temperature- and magnetic field-dependent resistivity (0.0055–2 Ω cm for W-rich and La-rich $LaWN_3$, respectively) are consistent with semiconducting behavior and are highly sensitive to cation stoichiometry, which may be related to amorphous impurities: metallic W or WN_x in W-rich samples and insulating La_2O_3 in La-rich samples. The fractional magnetoresistance is linear and small, consistent with defect scattering, and a W-rich sample has n-type carriers with high densities and low mobilities. We demonstrate a photoresponse in $LaWN_3$: The resistivity of a La-rich sample is enhanced by ∼28% under illumination and at low temperature, likely due to a defect trapping mechanism. The physical properties of $LaWN_3$ are highly sensitive to cation stoichiometry, like many oxide perovskites, which therefore calls for precise composition control to utilize the interesting properties observed in this nitride perovskite.

DOI: 10.1103/PhysRevMaterials.7.084411

I. INTRODUCTION

The perovskite crystal structure, first described for oxides by Goldschmidt and Megaw [1,2], is the largest and arguably the most flexible and useful family of crystalline materials. Perovskite and perovskite-derived materials display a staggering array of interesting ground states and functional properties, including high-temperature superconductivity in Ruddlesden-Popper layered cuprates, ionic and electrical conductivity in solid oxide fuel cells, ferroelectricity and dielectric behavior, and the photovoltaic effect in halide perovskites. Although many new ternary nitrides have recently been predicted, synthesized, and characterized [3,4]—including a number of antiperovskite nitrides (M_3NE) [5]—phase-pure nitride perovskites have proven significantly less accessible, despite intriguing calculated physical properties. The first nitride perovskite, $TaThN_3$, was reported in 1995, although the amount of oxygen incorporation was not characterized [6]. It is predicted to be semiconducting, have a large Seebeck coefficient, and be a topological insulator [7,8], although little follow-up experimental work has been reported. In addition, many oxynitride perovskites have been synthesized with a wide variety of properties, from electrochemical activity to colossal magnetoresistance [6,9–14], highlighting the possibility of uncovering interesting and potentially functional properties in the nearly unknown phase space of fully nitrided perovskites.

Recent work has reignited the search for nitride perovskites, spurred not only by experimental work on oxynitrides but also by computational studies showing that rare earth-based compositions should be stable—or metastable, but synthetically accessible—and exhibit interesting physics, including magnetic and ferroelectric properties [15–18]. These studies identified in particular the $REWN_3$ and

*rebecca.smaha@nrel.gov

†andriy.zakutayev@nrel.gov

Published by the American Physical Society under the terms of the Creative Commons Attribution 4.0 International license. Further distribution of this work must maintain attribution to the author(s) and the published article's title, journal citation, and DOI. Open access publication funded by the National Renewable Energy Laboratory (NREL) Library, part of a national laboratory of the U.S. Department of Energy.

REReN_3 (*RE* = rare earth) families as the most likely to form a perovskite structure. Follow-up density functional theory (DFT) calculations on $LaWN_3$ using hybrid functionals predicted that it should be a ferroelectric semiconductor with its ground-state structure as polar space group *R*3*c*, a large spontaneous polarization (∼61 μC/cm^2), and a band gap of 0.9–2 eV [15,19–24]. We previously successfully synthesized $LaWN_3$ as an oxygen-free perovskite in thin film form using radio frequency (RF) co-sputtering with plasma-activated nitrogen [25]. Recently, $LaWN_3$ was synthesized in bulk using high-pressure solid-state metathesis to increase the chemical potential of nitrogen, requiring 5 GPa and 1300 °C [23]. Rietveld refinements could not distinguish between polar, rhombohedral *R*3*c* symmetry and tetragonal $I\bar{4}$ [25] or cubic *Pm*-3*m* symmetry [23]. However, the large piezoelectric response measured in thin film $LaWN_3$ (effective piezoelectric strain coefficient $d_{33,f} \approx 40$ pm/V) confirms the calculated polar *R*3*c* symmetry and properties [25]. Attempts to measure a ferroelectric response in these films were unsuccessful due to large leakage currents, implying that more in-depth study of the optical and electronic properties is necessary.

Three additional rare-earth nitride perovskites have recently been reported. Similar thin film deposition methods yielded $CeWN_3$ and $CeMoN_3$ [26], finding that a competing fluorite phase was often present as an intermediate in the crystallization pathway from amorphous material to perovskite; heating the substrate during deposition or *ex situ* annealing in flowing N_2 were necessary to crystallize the perovskite phases of $CeWN_3$ and $CeMoN_3$, respectively. $CeMoN_3$ is antiferromagnetic below $T_N \approx 8$ K, while $CeWN_3$ is paramagnetic down to $T = 2$ K; both have large, negative Weiss temperatures, suggesting strong magnetic frustration. In addition, bulk $LaReN_3$ was synthesized using high-pressure techniques; interestingly, it required higher pressure (8 GPa and 1000–1200 °C) to stabilize compared to $LaWN_3$ [27] even though calculations suggested it should be slightly more stable than $LaWN_3$ [15]. $LaReN_3$ was reported to have metallic transport and exhibit Pauli paramagnetism.

In this article, we report on the structure and optoelectronic properties of thin film $LaWN_3$, employing combinatorial techniques to correlate these properties with stoichiometry. We report a two-step synthesis that utilizes RF substrate bias instead of an activated nitrogen plasma, as reported previously, followed by *ex situ* annealing. We investigate the crystal structure and composition of the combinatorial films produced by this method, studying the trends in crystallinity and texture with composition. The measured optical absorption onset and resistivity are consistent with semiconducting behavior and are highly sensitive to cation stoichiometry, which may be related to amorphous impurities: metallic W or WN_x in the W-rich samples and insulating La_2O_3 in the La-rich samples. The fractional magnetoresistance is linear and small, consistent with impurity scattering. We demonstrate a photoresponse in $LaWN_3$; the resistivity is enhanced at low temperature, likely due to a trapping mechanism.

II. METHODS

Experimental data used by this study have been analyzed using the COMBIgor software package [28] and are publicly available in the National Renewable Energy Laboratory (NREL) high-throughput experimental materials database (see also [29,30]).

A. Synthesis

Thin films of $LaWN_3$ were deposited using radio-frequency (RF) co-sputtering from elemental targets on 5.08 cm magnetrons in a vacuum sputtering chamber with a base pressure of approximately 2×10^{-7} Torr. The powers used were 50 W or 54 W (W, 99.95%) and 73 W (La, 99.5%). Deposition occurred at a pressure of 4 mTorr under 5 sccm of Ar and 10 sccm of N_2 (99.999%) gases. The substrate was heated to approximately 700 °C, and a cryogenic sheath was employed to trap adventitious oxygen or water during deposition. The source targets were presputtered for 90 or 120 minutes with the substrate shutter closed, followed by a 80 or 180 min deposition with a RF substrate bias (50 W). Immediately after deposition, the films were annealed for 30 min at 700 °C (without sputtering or substrate bias) under 10 sccm of N_2 at a pressure of 21.5 mTorr. Films were grown using the same conditions on two types of 5.08 × 5.08 cm substrates for different measurements: p-type Si(100) (pSi) substrates with either native or 100nm SiO_2 layers and sapphire (Al_2O_3) substrates. All substrates had a thin film of W on the back as a refractory metal to improve substrate heating. This was removed from the sapphire substrates with H_2O_2 prior to optical measurements.

After removal from the sputtering chamber and initial structural and compositional characterization, the films were annealed in a ULVAC MILA-3000 rapid thermal annealing (RTA) furnace under flowing N_2. The films were heated over 12 min to 800 °C and held at 800 °C for 10 min, followed by rapid cooling.

B. Composition and structural characterization

Cation composition was measured with x-ray fluorescence (XRF) using a Fischer XUV XRF under vacuum (∼1 Torr) using a model calibrated for pSi substrates (see Ref. [25]). For samples grown on sapphire substrates, the composition was assumed to be the same as pSi witness substrates. Oxygen and nitrogen contents were measured with Auger electron spectroscopy (AES) sputter depth profiling on a Physical Electronics 710 AES system. A 10 kV, 10 nA primary beam was used. Sputtering was performed with a 2-kV Ar^+ beam. Nitrogen AES sensitivity factors were determined from binary metal nitride powders, and metal AES sensitivity factors were determined as described previously [31] using one ungraded film grown on a pSi substrate for which the metal ratios were known from XRF. Oxygen was quantified with an AES sensitivity factor from the analysis software package (Physical Electronics MultiPak v9.6.1.7). Direct spectra were numerically differentiated and quantified within MultiPak.

Laboratory x-ray diffraction (XRD) patterns were collected with Cu K_α radiation on a Bruker D8 Discover diffractometer that allowed spatial mapping across the compositionally-graded thin films. Select samples grown on sapphire substrates were also evaluated at beamline 11-ID-B at the Advanced Photon Source, Argonne National Laboratory. These

synchrotron XRD data were collected in grazing incidence geometry with a wavelength of 0.1432 Å. LeBail fits were performed using the GSAS-II software suite [32].

Samples for cross-sectional scanning electron microscopy (SEM) were prepared by mechanical cleaving immediately before loading them into the SEM vacuum chamber. Cross-sectional micrographs were acquired on a Hitachi S-4800 SEM operating at 3 kV accelerating voltage in secondary electron imaging mode.

C. Optical, transport, and magnetic characterization

Transmission UV-vis optical spectroscopy spectra were collected on a Agilent Cary-6000i system with spot size approximately 3 mm^2 on films grown on sapphire substrates. Absorption coefficients were determined from these data together with thicknesses extracted from the SEM data. Carrier densities ($|n|$) were extracted by modeling the peak at low energy as the plasma frequency ω_p; see Eq. (1) below.

Spectroscopic ellipsometry data were acquired at 65°, 70°, and 75° incident angles on a single row of a select annealed combinatorial sample (11 points per row) using a J.A. Woollam Co. M-2000 variable angle ellipsometer. The sample was grown on a crystalline pSi(100) substrate and was approximately 750–800-nm thick. CompleteEASE software (version 6.63) was used to model the data by fitting the real and imaginary parts of the dielectric function with a single layer model consisting of the $LaWN_{3-y}$ film. No substrate was necessary in the model due to the $LaWN_{3-y}$ film transmitting no photons through to the silicon substrate. The $LaWN_{3-y}$ film was modeled using two oscillators: (1) a parametric semiconductor oscillator (PSemi-Tri), which is an established model for accurately fitting the imaginary part of the dielectric function of crystalline semiconductor materials while maintaining Kramers-Kronig consistency [33], and (2) a Drude oscillator to model the subgap absorption below 2 eV.

For electrical transport, ∼370-nm thick films were deposited as cloverleafs on a sapphire substrate. 10 nm of Ti and 100 nm of Au were deposited via electron-beam evaporation as electrical contacts for the Van der Pauw measurement. The sheet and Hall resistances (R_S and R_{xy}) were measured as a function of temperature and applied magnetic field in a Quantum Design Physical Property Measurement System. All reported magnetoresistances (Hall resistances) are symmetrized (antisymmetrized) as a function of applied field. Temperature-dependent photoresistivity was additionally measured down to $T = 100$ K using a Lake Shore Cryotronics Model 8425. Samples were illuminated with a G2V Pico LED solar simulator with a 365–1450-nm AM1.5G spectrum. We verify its intensity to be 23 mW/cm^2 using a reference solar cell.

Magnetic properties were measured on a $LaWN_{3-y}$ sample and a $CeWN_{3-y}$ sample via superconducting quantum interference device (SQUID) magnetometry in a Quantum Design Magnetic Properties Measurement System (MPMS3). The films were measured from 1.8–300 K under applied fields from –7 to +7 T. The measured $LaWN_{3-y}$ film was an approximately 5 × 5 mm piece of a combinatorial film grown on a pSi substrate with a thin layer of metallic W on the back. It was approximately 750-nm thick with composition La/(W+La) = 50.6%, as measured by XRF. The measured $CeWN_{3-y}$ film was an approximately 5 × 5 mm piece of a combinatorial film grown on a pSi substrate; it was approximately 150–200-nm thick with cation composition Ce/(W+Ce) ≈ 51% [26]. To isolate the signal of the films, bare substrates were also measured and subtracted. The resulting signal for $CeWN_{3-y}$ was scaled to match the approximate volume of the $LaWN_{3-y}$ film.

D. Computations

We used first-principles density functional theory (DFT) to perform structural relaxation of $LaWN_3$ in a $R3c$ unit cell with 10 atoms. All DFT calculations were performed with the Vienna *ab initio* Simulation Package (VASP) [34,35] using projector augmented wave (PAW) pseudopotentials [36] to describe the core electrons. The wave functions were expanded as plane waves with an energy cutoff of 340 eV. The structural relaxations were performed within the generalized gradient approximation (GGA) of Perdew-Burke-Erzenhof (PBE) as the exchange correlation functional. A Hubbard on-site energy correction of $U = 3$ eV was applied to the d orbitals of La and W, following the methodology in Refs. [37,38]. For the relaxed structure, we calculated the electronic structure using the tetrahedron integration scheme on a dense Γ-centered 8 × 8 × 8 Monkhorst-Pack k-point grid. The density-of-states effective mass (m^*_{DOS}) was determined from the DOS within the single parabolic band approximation, such that the parabolic band reproduces the same number of states as the DOS within a 100 meV energy window from the relevant band edges. The band effective mass (m^*_{b}) was calculated within the parabolic and isotropic band approximation: $m^*_{\mathrm{b}} = m^*_{\mathrm{DOS}}\, N_b^{-2/3}$, where N_b is the band degeneracy [39]. The static dielectric constant (ϵ_∞), used to determine the plasma frequency, was calculated using density functional perturbation theory. The underestimation of the band gap with GGA-PBE was remedied by computing band edge shifts from GW quasiparticle energies [40]. We used DFT wave functions as initial wave functions for the GW calculations. GW eigenvalues were then iterated to self-consistency, removing the dependence on the single-particle Kohn-Sham energies. The input DFT wave functions were kept constant during the GW calculations, which allows the interpretation of the GW eigenenergies in terms of energy shifts relative to the Kohn-Sham energies. The GW quasiparticle energies were calculated using a Γ-centered 8 × 8 × 8 k-point grid.

III. RESULTS AND DISCUSSION

A. Growth and composition

Thin films of $LaWN_3$ were grown via RF co-sputtering at high temperature (∼700 °C) on pSi and sapphire (Al_2O_3) substrates to enable a range of property measurements. Combinatorial growth was performed targeting a narrow region of phase space around $LaWN_3$. Throughout this paper, we use $LaWN_{3-y}$ to refer to the combinatorial films, which generally have a small amount of N deficiency ($y \approx 0.5$), as noted in Ref. [25]. The growths yielded films with a composition gradient roughly 45% < La/(W+La) <54% (i.e., $La_{0.9}W_{1.1}N_{3-y} - La_{1.08}W_{0.92}N_{3-y}$).

Cation composition La/(W+La) was mapped across the combinatorial samples using x-ray fluorescence (XRF), and several points were additionally measured with Auger electron spectroscopy (AES) depth profiling. Consistently higher La/(W+La) values were measured via XRF in samples grown on transparent substrates (i.e., sapphire) compared to on pSi substrates, despite similar optical and electrical properties; to correct this, the AES measurements were calibrated with the XRF results from the films grown on pSi substrates. Calibrated AES atomic % depth profiles are shown in Fig. S1 within the Supplemental Material (SM) [41]. The overall calibrated composition derived from AES for the sample with mean La/(W+La) = 49.0(4)% on a sapphire substrate is $La_{0.98}W_{1.02}N_{2.33}O_{0.07}$ (Fig. S1B within SM [41]), calculated assuming that the cation stoichiometry should sum to two. Similarly, a sample on a Si substrate with mean La/(W+La) = 50.6(1)% has overall composition $La_{1.01}W_{0.99}N_{2.52}O_{0.07}$ (Fig. S1E within SM [41]). The observed nitrogen substoichiometry is consistent with previous reports [25], and may be due to N loss during AES depth profiling.

Cation stoichiometry La/(W+La) and oxygen anion content O/(O+N) AES depth profiles of several spots along a combinatorial film grown on a sapphire substrate are shown in Fig. 1, and analogous depth profiles along a film grown on a pSi substrate are in Fig. S2 within SM [41]. The positions along the sample library at which AES depth profiles were measured are shown as the square symbols in the inset to Fig. 1(b). The La content La/(W+La) is relatively flat through the film for all spots measured [Fig. 1(a)]. The oxygen content, represented in Fig. 1(b) as O/(O+N), is low for all samples measured, below ∼7%. The oxygen spectra are shown in Fig. S3 within SM [41]. For the La-rich sample with mean La/(W+La) = 52.5(4)%, the oxygen content is highest near the surface and lowest near the substrate interface, consistent with slight oxidation due to air exposure post-growth. For the W-rich sample with mean La/(W+La) = 48.8(7)%, the oxygen content rises slightly near the substrate interface, to ∼10%. This may be due to either to pinholes allowing air to enter the interface between the sapphire substrate and the $LaWN_{3-y}$ film, or to small amounts of oxygen diffusing into the film from the sapphire substrate. Optical SEM images of spots along combinatorial films grown on both sapphire and pSi substrates after annealing are shown in Fig. S4 within SM [41].

We investigated whether $LaWN_{3-y}$ could be synthesized without an activated nitrogen plasma created with a nitrogen plasma source, which was used in the first report of thin film $LaWN_3$ [25] but is not standard equipment. We found that using a RF substrate bias, which controls the voltage of the substrate relative to the plasma, at a power of 50 W during deposition aided in forming nanocrystalline films that could then be crystallized via *ex situ* annealing, as shown in Fig. 2. In addition, RF substrate bias is a significantly more common capability compared to a nitrogen plasma source. The nanocrystalline films produced by this method contrast with the polycrystalline films observed in Ref. [25] as a result of high-temperature growth with an activated nitrogen plasma in the same sputtering chamber; we attribute the difference either to a slight decrease in the maximum temperature achievable by the substrate heater or to the lower chemical potential of

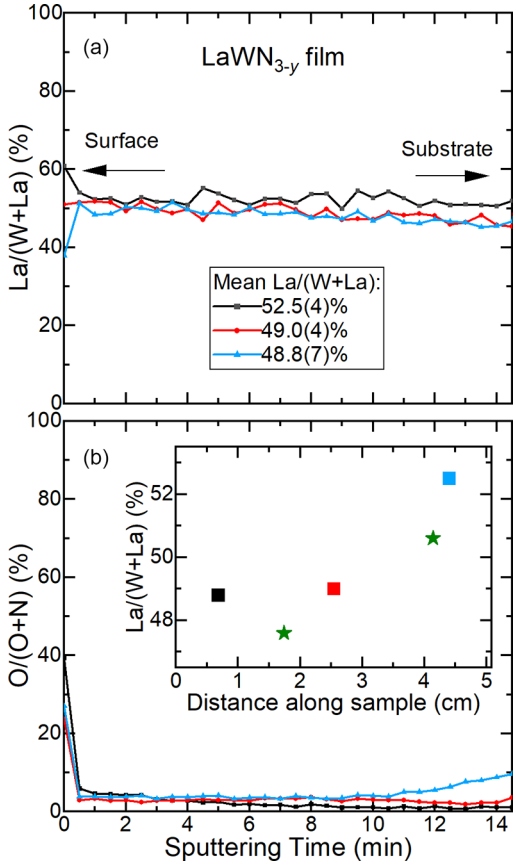

FIG. 1. AES depth profiles of several spots along a combinatorial $LaWN_{3-y}$ film grown on a sapphire substrate. (a) La cation content La/(W+La) and (b) Oxygen anion content O/(O+N) as a function of sputtering time. The inset in (b) shows the position of the three spots measured by AES across the combinatorial sample (square symbols) as well as the two spots measured in synchrotron XRD (star symbols, see discussion below). The cation ratio for the XRD spots was measured with XRF.

nitrogen with the RF substrate bias. To compensate for this, we performed *ex situ* anneals in flowing N_2 at 800 °C for 10 min; this crystallized the perovskite phase, as shown in Fig. 2(b). The success of RF substrate biasing for $LaWN_{3-y}$ is consistent with previous results in other materials families; it has been found to increase reactive gas content in various films [42], affect the film stress [43], and in particular for many sputtered nitride materials (including TiN and AlN) it has improved the electrical properties and film morphology [44].

B. Crystal structure

Following the first synthesis step (deposition), we performed laboratory x-ray diffraction (XRD) on the combinatorial $LaWN_{3-y}$ films, as shown in Fig. 2(a). An intense but relatively broad peak at approximately $2\theta \approx 31°$ ($Q = 2.22$ Å^{-1}) is observed in most of these as-grown XRD patterns; this is indicative of nanocrystalline perovskite formation. The average FWHM of this peak is 1.35(4)° 2θ, extracted from fits of the XRD data to a pseudo-Voigt function (see Table S1 within SM [41]). Samples with La/(W+La)

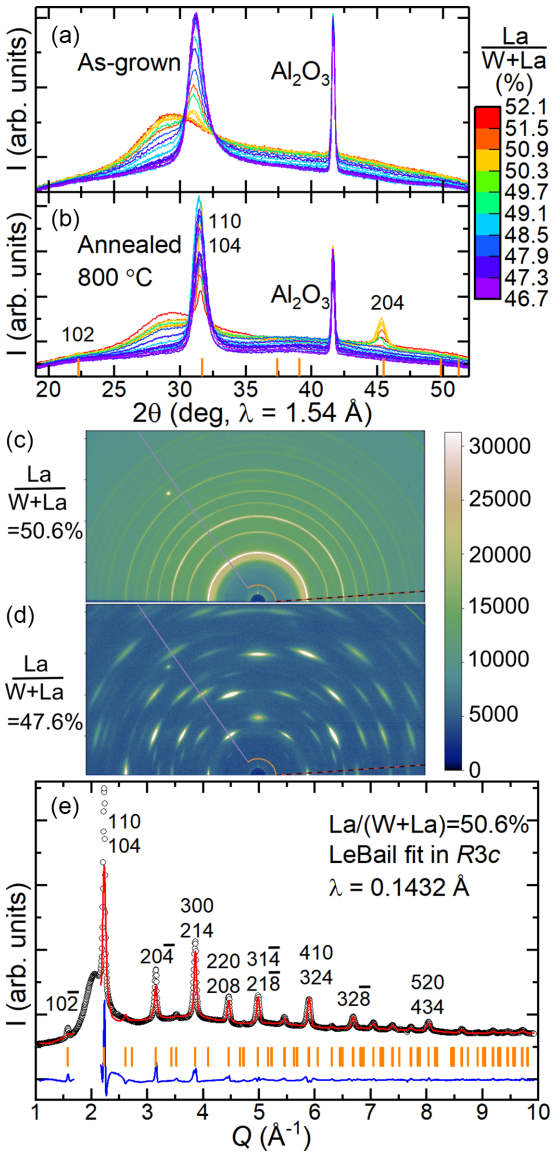

FIG. 2. [(a), (b)] Laboratory XRD of a combinatorial $LaWN_{3-y}$ film grown on a sapphire substrate as a function of La/(W+La): (a) as-grown, and (b) after annealing at 800 °C in flowing N_2. Calculated reflections for $LaWN_3$ are shown in (b). The sharp peak at $2\theta = 41.6°$ is from the sapphire substrate. [(c), (d)] 2D detector images of grazing incidence XRD of (c) La-rich [La/(W+La) = 50.6%] and (d) W-rich [La/(W+La) = 47.6%] $LaWN_{3-y}$ combinatorial films collected at APS beamline 11-ID-B with wavelength $\lambda = 0.1432$ Å. The films were grown on sapphire substrates, and the lines show the integration limits. The locations along the combinatorial sample at which these synchrotron XRD patterns were measured are shown in the inset of Fig. 1(b). (e) LeBail fit in space group *R*3*c* of the integrated synchrotron XRD data collected on the sample with La/(W + La) = 50.6% shown in panel (c).

$\gtrsim$49% La content also display a broad hump centered around $2\theta \approx 29°$ ($Q = 2$ Å^{-1}), which corresponds roughly to the main diffraction peak of La_2O_3, likely indicating the presence of nanocrystalline LaN or La_2O_3. The most La-rich [La/(W+La) $\gtrsim$51%] samples display only this broad peak without a perovskite peak. The laboratory 2D detector data (Fig. S6A within SM [41]) show that this broad peak in La-rich samples is relatively polycrystalline, displaying little to no crystallographic texture. The perovskite-related peak in W-rich samples, visible on the edges of the detector images, is textured; this is accompanied by an increase in the FWHM (see Figs. S6 and S7 within SM [41]).

Upon *ex situ* annealing in flowing N_2 at 800 °C, additional perovskite peaks appear; this is shown for laboratory XRD in Fig. 2(b) and for synchrotron grazing incidence XRD measured at beamline 11-ID-B at the APS in Figs. 2(c)–2(e). The locations along the sample library at which synchrotron XRD was measured are shown in the inset of Fig. 1(b). As a result of this crystallization, laboratory XRD [Fig. 2(b)] reveals that the main perovskite peak—corresponding to the (110) and (104) reflections—"snaps" to a more constant position of 31.501(2)° 2θ and a narrower FWHM of 0.915(7)° 2θ. The positions and FWHM are shown in Fig. S7 within SM [41], and the average values are in Table S1 within SM [41]. This change is particularly evident in the La-rich samples; see Figs. 2(a) and 2(b) and S5 (within SM [41]) as well as the 2D detector images in Figs. S6A and S6B within SM [41]. All samples across the full range of cation stoichiometry La/(W+La) present in this combinatorial sample now display this main perovskite peak, although the trend from polycrystallinity in the La-rich samples to texture in the W-rich samples is still observed.

Similar behavior as a result of annealing is observed in samples grown on pSi substrates, as shown in Figs. S5 and S6C–S6D within SM [41]. No significant differences were observed between $LaWN_{3-y}$ grown on sapphire and pSi substrates in the peak position or FWHM in 2θ (Q). However, in the radial direction (χ), the average FWHM of the perovskite peak is narrower for films grown on sapphire [8.2(1)°] compared to pSi [10.5(1)°]; this is visible in Fig. S6 within SM [41].

A LeBail fit was performed on the integrated synchrotron data for the polycrystalline sample with La/(W+La) = 50.6% in space group *R*3*c*, as shown in Fig. 2(e). The refined lattice parameters are $a = 5.637(6)$ and $c = 13.82(1)$, similar to the lattice parameters found in Refs. [23,25]. Some amorphous or nanocrystalline La_2O_3 is still present in the La-rich samples, as seen by the broad peak at $2\theta \approx 29°$ in Fig. 2(b) and $Q \approx 2$ Å^{-1} in Fig. 2(e), but the overall amount appears lower compared to the as-grown samples, suggesting that at least some of it has been incorporated into the perovskite structure. However, as some La is tied up in the La_2O_3 impurity amorphous phase, the actual perovskite phase in the La-rich samples may be La poor. An extremely broad background centered at $2\theta \approx 40°$ that emerges in the W-rich annealed samples additionally suggests that a small amount of nanocrystalline metallic W may be present. We note that polycrystalline $LaWN_{3-y}$ films synthesized previously by a two-step process (involving room-temperature growth with an activated nitrogen plasma followed by an *ex situ* anneal at 900 °C in flowing N_2) showed significant amounts of crystalline metallic W and small amounts of crystalline La and possibly WN [25]. However, previous one-step growth at high temperature with an activated nitrogen plasma yielded phase-pure $LaWN_{3-y}$ films, albeit with preferred orientation [25]. Therefore, the crystallinity of these impurity phases is

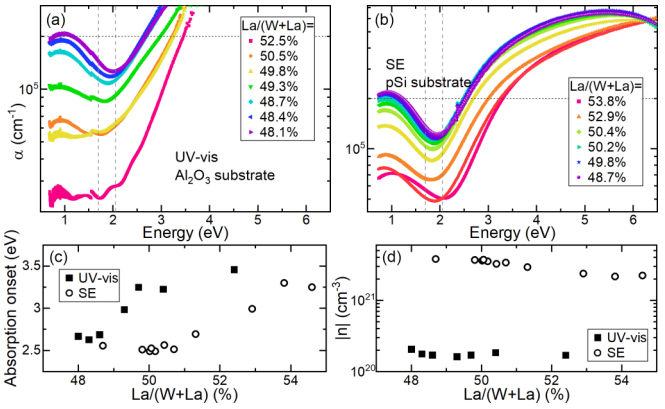

FIG. 3. Absorption coefficient α extracted from (a) UV-vis data of a combinatorial $LaWN_{3-y}$ film grown on a sapphire substrate, and (b) spectroscopic ellipsometry (SE) data of a combinatorial $LaWN_{3-y}$ film grown on a pSi substrate. The horizontal dashed line is the chosen optical absorption onset. The vertical dashed lines represent the calculated band gaps at 1.7 eV (indirect) and 2.05 eV (optical). (c) Absorption onsets extracted from UV-vis and SE data of $LaWN_{3-y}$ grown on sapphire and pSi substrates, respectively. The absorption onset is calculated as the energy at which each curve intersects with $\alpha = 2 \times 10^5$ cm^{-1} [see dashed lines in panels (a) and (b)]. (d) Carrier densities $|n|$ extracted from the low-energy regions of the SE and UV-vis data.

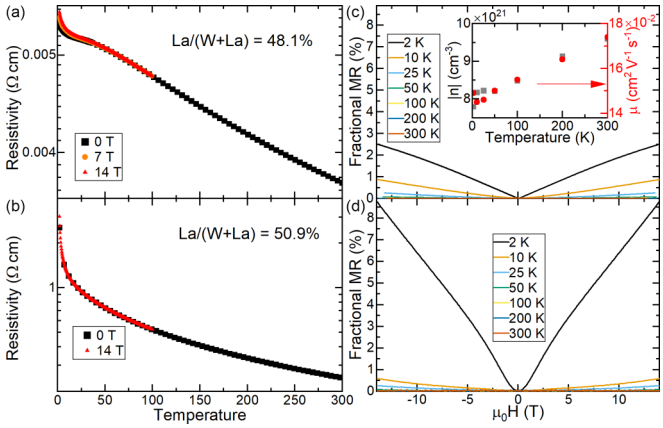

FIG. 4. Temperature-dependent resistivity (R_S) of $LaWN_{3-y}$ films with (a) La/(W+La) = 48.1% and (b) measured under several applied fields. (c) Fractional magnetoresistance (MR) of $LaWN_{3-y}$ films with (c) La/(W+La) = 48.1% and (d) La/(W+La) = 50.9% measured at several temperatures. The inset in (c) shows the extracted carrier densities (n) and mobilities (μ) as a function of temperature.

heavily dependent on synthesis method. The two-step technique employed here yields a range of crystalline textures for the $LaWN_{3-y}$ phase dependent on stoichiometry, but the impurity phases are reliably amorphous or nanocrystalline.

C. Optical properties

To probe the optical properties of these films, we performed UV-vis measurements across a combinatorial $LaWN_{3-y}$ film grown on a sapphire substrate and spectroscopic ellipsometry (SE) measurements across a film grown on a pSi substrate. The absorption coefficients (α) extracted from both measurements are shown in Figs. 3(a) and 3(b), respectively. Modeling the SE data revealed that a few hundred nm of $LaWN_{3-y}$ does not transmit photons. The two techniques display similar trends overall, with the La-rich compositions exhibiting absorption onsets at higher energies than the W-rich compositions.

To quantify the trends with composition yet avoid the errors endemic to Tauc analyses, we define an optical absorption onset as the energy when $\alpha = 2 \times 10^5$, shown in Fig. 3(c). While some variation exists between the onsets extracted from the UV-vis and SE data, both techniques yield low onsets for La/(W+La) <50%, at approximately 2.5 eV. The absorption onset is highly sensitive to composition. It increases with higher La/(W + La) values, plateauing at about 3.3–3.5 eV. The behavior at La/(W+La) <50% is likely due to microscopic metallic W or WN_x impurities in the W-rich region, while the behavior in the La-rich region is likely dominated by insulating La_2O_3 impurities. This is accompanied by a color change from translucent yellow-brown to black (as shown in Ref. [25]). We used the GW approximation to calculate an indirect band gap of 1.70 eV and an optical (vertical transition) band gap = 2.05 eV (see Sec. II for details), which is in the range of band gaps (1.59–2.0 eV) obtained from DFT calculations using hybrid functionals [15,19,20,23,24]. The GW-calculated band gap is for defect-free, bulk $LaWN_3$ and does not account for the cation off-stoichiometry observed in experiments. However, these values are slightly different than those reported for the bulk, high-pressure sample (1.2 eV direct and 2.2 eV indirect), perhaps reflecting different defects [23]. Due to the choice of $\alpha = 2 \times 10^5$ as a cutoff, the extracted absorption onsets are higher than the calculated band gap, but the trends should be consistent.

Significant subgap absorption is evident for W-rich samples in the 1–2 eV region in both the UV-vis and SE data [Figs. 3(a) and 3(b)]. In the SE data, this region was modeled with a Drude oscillator, allowing the extraction of carrier densities ($|n|$), as shown in Fig. 3(d). These are on the order of $|n| \approx 2$–4×10^{21} cm^{-3}, which is high but consistent with the large observed absorption below the gap. The densities are higher for W-rich samples. The peak in the low-energy UV-vis absorption can be interpreted as the plasma frequency (ω_p); carrier densities ($|n|$) were extracted as

$$|n| = \frac{\omega_p^2 m^* \epsilon_\infty \epsilon_0}{e^2} \quad (1)$$

where m^* is the electron effective mass and ϵ_∞ is the static dielectric constant. Here, we use DFT-calculated $m^* = 0.836\ m_e$ and $\epsilon_\infty = 13.61$ (see Sec. II for details). These values are similar to those calculated with DFT methods [22,24]. This calculation yields $|n|$ values on the order of $|n| \approx 2 \times 10^{20}$ cm^{-3}, slightly lower than the values extracted from the SE fitting and exhibiting fewer trends with composition.

D. Electrical transport

We measured the temperature and magnetic field-dependent electrical transport of $LaWN_{3-y}$ films for the first time. Figure 4 summarizes the electrical transport measured

on two $LaWN_{3-y}$ samples grown on sapphire substrates, a W-rich sample [La/(W+La) = 48.1%, Figs. 4(a) and 4(c)] and a La-rich sample [La/(W+La) = 50.9%, Figs. 4(b) and 4(d)]. Strikingly, the measured resistivities (ρ) of the two samples—which have a composition difference of only La/(W+La) ≈3%—differ by approximately two orders of magnitude. The W-rich sample exhibits temperature-dependent resistivity consistent with degenerately doped semiconducting behavior [Fig. 4(a)]. The La-rich sample is approximately two orders of magnitude more insulating and exhibits a temperature dependence characteristic of an insulator. This difference in resistivity is large given the small difference in cation ratio between the two samples, less than 3% La/(W+La). While the samples measured here do contain significant levels of defects, no clear superconducting transition is seen below $T \approx 6$ K in either sample, implying low amounts of—or very amorphous—WN_x impurities, in contrast to the reported bulk $LaReN_3$ sample that contained superconducting ReN_x impurities [27].

The behavior below $T \approx 50$ K in the W-rich sample [Fig. 4(a)] may be due to freezing out hopping between conductive regions of impurities such as amorphous or nanocrystalline W or WN_x. This low-temperature region was measured in several applied fields; the curves deviate from the $\mu_0 H = 0$ T data below approximately $T = 50$ K. Following prior studies [45,46], we investigated several models to fit the low-temperature, zero-field region (below $T = 46$ K), including a mix of defect-mediated contributions in the form of Mott 3D variable range hopping (VRH) and band-mediated contributions in the form of an Arrhenius model: $\rho(T) = \rho_0 + Ae^{\frac{\Delta E}{k_B T}} + Be^{(\frac{T_0}{T})^{1/4}}$. However, the Arrhenius contribution did not improve the fit, so we fit the data with only the 3D VRH model (see Fig. S8 within SM [41]). We hypothesize that at low temperatures, the conduction is dominated by defect states, and as the temperature decreases the thermal energy becomes competitive with the energy of hopping. The temperature trends in the extracted carrier densities (n) and mobilities (μ), discussed below, are consistent with this hypothesis [see inset of Fig. 4(c)].

With only a small change in cation ratio (<3%), the La-rich sample [La/(W+La) = 50.9%] is more insulating than the W-rich sample by approximately two orders of magnitude [Fig. 4(b)]. The low-temperature behavior is characteristic of an insulator, consistent with the likely impurities of La_2O_3 or LaN rather than conductive W or WN_x. We note that the presence of La_2O_3 impurities implies that the perovskite phase in this nominally La-rich sample may be La poor, implying a potential source of unintentional electrons from N vacancies and O substitution. We also attempted fitting the low-temperature behavior ($T < 38$ K) with a mixed Arrhenius and 3D VRH model. Similar to the W-rich sample, the Arrhenius component did not fit the data well (see Fig. S8 within SM [41]). The extracted 3D VRH coefficients (B) from fitting these two samples differ by four orders of magnitude (~2.9E–4 for the W-rich sample and ~2 for the La-rich sample), reflecting the difference in their resistivities.

Magnetic field-dependent resistance was measured at a range of temperatures, shown as the fractional magnetoresistance (FMR = $[R(\mu_0 H) - R(0)]/R(0) \times 100$) in Figs. 4(c) and 4(d). At $T = 2$ K, the FMR of the W-rich sample [Fig. 4(c)] is linear and reaches approximately 2.5% at $\mu_0 H = 14$ T. The origins of this linear MR could be semi-classical or impurity/defect-driven [47–50]. The linear MR decreases quickly at higher temperatures and disappears by $T = 50$ K, consistent with the temperature-dependent results [Fig. 4(a)]. By measuring the Hall resistance (R_{xy}, Fig. S9 within SM [41]), we find that the W-rich film is n-type with a carrier density of $n = -7.8 \times 10^{21}$ cm^{-3} and a low-carrier mobility of $\mu = 0.149$ cm^2 V^{-1} s^{-1}) at $T = 2$ K. The trends with temperature are shown in the inset of Fig. 4(c). This n-type behavior likely arises from nitrogen vacancies and oxygen defects, and it is consistent with observed behavior in many nitrides [51,52]. The extracted $|n|$ values are comparable to the sheet carrier densities extracted from the optical measurements (Fig. 3), although there is better agreement with the SE values than with the UV-vis values. The FMR of the La-rich sample [Fig. 4(d)] is linear and larger than the W-rich sample, ~9% at $T = 2$ K.

E. Photoresponse

As we calculated a bandgap for $LaWN_3$ of 1.7 eV (indirect) using the GW approximation, we measured the temperature-dependent resistivity of these two samples of $LaWN_{3-y}$ under AM1.5G spectrum illumination in a different chamber. The light that reached the sample location was calibrated with a known CIGS solar cell, revealing that the highest effective illumination was approximately 23 mW/cm^2. The dark resistivities of both samples between $T = 100$–300 K, shown in Fig. 5(a), are consistent with the PPMS measurements. The change in slope at $T \approx 225$ K is an instrumental artefact; it has been observed across a range of samples on several substrates [51–53].

Under illumination, the resistivities of both samples decrease. This effect is most pronounced at lower temperatures, below approximately $T = 175$ K. We note that due to the low-illumination intensity (~0.25 suns), thermal effects should be weak. We examined the dependence of resistivity upon illumination intensity at $T = 100$ K, as shown in Fig. 5(b), finding a smooth evolution up to the highest possible intensity. For the W-rich sample, the change ($[\rho(I) - \rho(0)]/\rho(0) \times 100$) is approximately 5% at the highest illumination, while for the La-rich sample the change is ~28%. We note that the switching dynamics of this photoresponse are slow, suggesting that the underlying behavior is not carrier recombination but more likely trapping and de-trapping of defect states at the surface of the film. This hypothesis is consistent with the observed stronger response at low temperatures: the energy of trapping must reach rough equivalence with thermal energy at approximately 150–175 K, where the dark and illuminated resistivities merge. The different defects—and defect densities—in the W-rich sample (metallic W and WN_x) compared to the La-rich sample (insulating La_2O_3) likely contribute to the different degree of photoresponse (5% and 28%, respectively). Wavelength dependence measured at $T = 100$ K and low-illumination intensity (approximately 0.02–0.03 suns) showed no strong trends. These results are broadly consistent with recent computational work arguing that nitride perovskites are defect-intolerant semiconductors [24]. This is

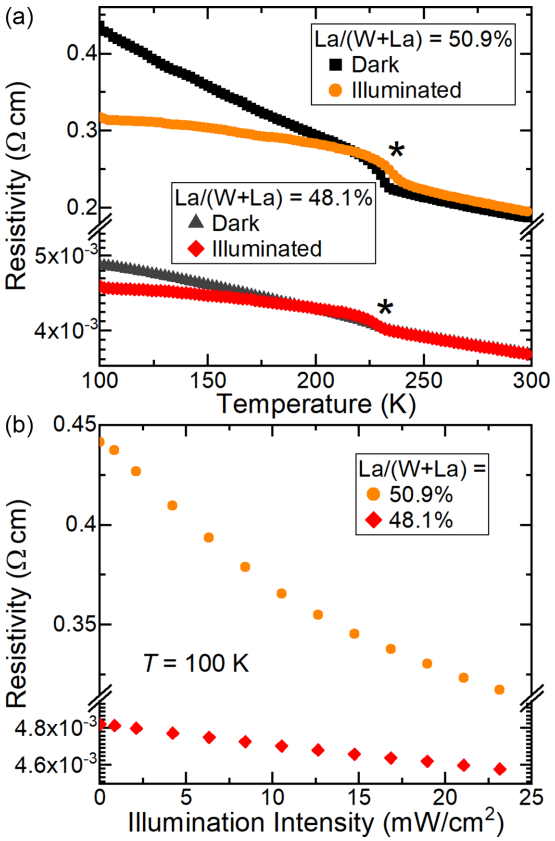

FIG. 5. (a) Temperature-dependent resistivity of two samples of $LaWN_{3-y}$ with La/(W+La) = 48.1% and La/(W+La) = 50.9% in the dark and under AM1.5G spectrum illumination at an intensity of 23 mW/cm^2. The change in slope at $T \approx 225$ K, marked with asterisks, is an instrumental artefact; it has been observed across a range of samples on several substrates [51–53]. (b) Resistivity as a function of illumination intensity of the AM1.5G spectrum.

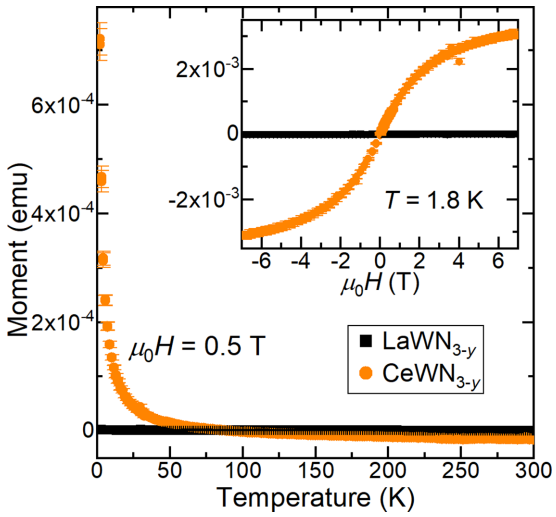

FIG. 6. Comparison of DC magnetic moment measurements at an applied magnetic field of $\mu_0 H = 0.5$ T for $LaWN_{3-y}$ and $CeWN_3$. Inset: Moment as a function of applied field at $T = 1.8$ K for $LaWN_{3-y}$ and $CeWN_3$. The substrate contribution has been subtracted from all data, and the resulting signal for $CeWN_3$ was scaled to match the approximate volume of the $LaWN_{3-y}$ film. The measured films have cation stoichiometries La/(W+La) = 50.6% and Ce/(W+Ce) = 51%, as measured by XRF, and were grown on a pSi substrate with W on the back ($LaWN_{3-y}$) and a pSi substrate ($CeWN_{3-y}$).

the first demonstration of photoresponse in $LaWN_{3-y}$ films, and further investigation will be required to fully understand the nature of the carrier dynamics and effects of defects in $LaWN_{3-y}$ films.

F. Magnetism

To check the magnetism of $LaWN_{3-y}$, we performed temperature-dependent DC moment measurements on a piece of a combinatorial $LaWN_{3-y}$ film grown on a pSi substrate at an applied magnetic field of $\mu_0 H = 0.5$ T, as shown in Fig. 6. The cation stoichiometry of this sample is approximately La/(W+La) = 50.6%, as measured by XRF. We compare it to the Ce analog, $CeWN_{3-y}$, which we recently reported as a new nitride perovskite that is paramagnetic down to $T = 2$ K [26]. Although the mass of these perovskite thin films cannot be quantified precisely, to yield the most quantitative comparison the substrate contribution for each sample (pSi with W on the back for $LaWN_{3-y}$ and SiN_x|pSi for $CeWN_{3-y}$) has been subtracted, and the resulting perovskite signal has been scaled to the same approximate film volume. We note, however, that the moment values are still approximate, and that both films may have some amorphous or nanocrystalline phase fraction in addition to the crystalline perovskite phase.

The measured moment for $LaWN_{3-y}$ is temperature-independent and very weakly positive at $\mu_0 H = 0.5$ T, while the $CeWN_{3-y}$ sample shows a much stronger paramagnetic response. The inset shows the field-dependent measurement at $T = 1.8$ K for both perovskites; similarly, the $LaWN_{3-y}$ response is very weak, while the $CeWN_{3-y}$ sample is paramagnetic. The slope of the $LaWN_{3-y}$ signal is nearly flat within the error bars, with a small ferromagnetic contribution at low fields that likely arises from sample holders and handling. A temperature-dependent scan was performed in a low field of $\mu_0 H = 0.0002$ T to check for a drop in resistance due to superconducting impurities, such as the ReN_x impurities observed in the bulk $LaReN_3$ synthesized via high-pressure techniques [27]; as shown in Fig. S10 within SM [41], none are observed down to $T = 1.8$ K.

For ideal $LaWN_3$, we expect diamagnetism consistent with La^{3+} and W^{6+}. Interestingly, although $LaReN_3$ should be paramagnetic due to Re^{6+}, it was reported to exhibit weak Pauli paramagnetism, consistent with its predicted and reported metallicity [17,27]. The magnetic behavior observed here for $LaWN_3$ is a very weak response—especially compared with $CeWN_{3-y}$, which exhibits paramagnetism consistent with the Curie law—that could be consistent with either diamagnetism or possibly Pauli paramagnetism from impurity phases. Comparing $LaWN_3$ with $LaReN_3$, $CeWN_{3-y}$, and $CeMoN_{3-y}$, which has a transition to long-range antiferromagnetism below $T_N \approx 8$ K [26], begins to illuminate broader trends in the magnetism of nitride perovskites. For the Ce perovskites, we were not able to experimentally determine whether the magnetism arises from Ce^{4+} or W^{5+}/Mo^{5+}, but the differences between them as well

as the weak behavior of both La perovskites suggest that the magnetic moment in nitride perovskites arises primarily from the *A* site.

IV. CONCLUSIONS

We have investigated the structural, optical, and electronic properties of combinatorial thin films of $LaWN_{3-y}$, one of the first oxygen-free nitride perovskites ever reported. As previous work on thin film $LaWN_{3-y}$ focused on its experimentally-proven piezoelectricity but encountered problems measuring a ferroelectric response due to large leakage current, a detailed investigation into its optoelectronic properties is necessary to better understand and subsequently control the underlying physics of $LaWN_{3-y}$. We grow combinatorial thin films on both silicon and sapphire substrates using a two-step process: a high-temperature deposition employing a RF substrate bias, yielding amorphous or nanocrystalline films, followed by an *ex situ* anneal at 800 °C in flowing N_2 that crystallizes the perovskite phase. Texturing is dependent on stoichiometry, with polycrystalline La-rich films and highly textured W-rich films. AES depth profiles demonstrate a low amount of oxygen through the film, confirming the viability of this synthesis method for producing nearly oxygen-free $LaWN_{3-y}$.

We find that the optical and electronic properties of thin film $LaWN_{3-y}$ are highly sensitive to stoichiometry. UV-vis spectroscopy and spectroscopic ellipsometry reveal that the absorption onset, which should display similar trends to the bandgap and carrier density, changes by ∼1 eV. In W-rich samples [La/(W+La) <50%], significant subgap absorption is observed, consistent with metallic W or WN_x impurities. We report the low-temperature resistivity of thin film $LaWN_{3-y}$ in applied magnetic fields from 0–14 T, revealing behavior consistent with a degenerately doped semiconductor in slightly W-rich $LaWN_{3-y}$ and insulating behavior in slightly La-rich $LaWN_{3-y}$. The fractional magnetoresistance is linear and small, consistent with defect scattering, and a W-rich sample exhibits n-type carriers with high electron densities $n \approx -8 \times 10^{21}$ cm^{-2} and low electron mobilities $\mu \approx 0.149$ cm^2/(V s) at $T = 2$ K. A photoresponse is observed: The resistivity decreases at low temperatures under solar spectrum illumination, and a larger effect is observed for the La-rich sample compared to the W-rich sample; this is consistent with a defect trapping mechanism. Magnetic moment measurements of $LaWN_{3-y}$ reveal a very weak magnetic response, consistent with expectations of the closed-shell configuration of the constituent ions.

The sensitivity of the measured structural and optoelectronic properties of $LaWN_{3-y}$ to cation stoichiometry suggests that it is a line compound, which is common in oxide perovskites. This has important implications for the successful realization of the physical properties of $LaWN_3$, including its high predicted ferroelectric response: Precise composition control, rigorous oxygen exclusion, and thorough characterization will be crucial to understand and prevent unwanted impurity phases and oxygen incorporation. For example, to reduce leakage for ferroelectric applications, films with a higher band gap—to avoid shunts through grain boundaries—are generally preferable. In light of these results, future work on ferroelectric $LaWN_3$ should focus on optimizing La-rich compositions, which we show have wider band gaps but prefer to grow polycrystalline. They may also be more likely to form with insulating phases at grain boundaries, affording low leakage, although improving materials quality and engineering defects will also be necessary. Overall, the semiconducting physical properties and sensitive composition dependence of $LaWN_3$ investigated here are likely generalizable to other members of this emerging materials family of nitride perovskites as a whole, which has been the focus of many computational studies but only a few experimental reports. Thus, we provide a path forward to understanding the intrinsic physics of this new materials family and experimentally realizing its predicted properties.

ACKNOWLEDGMENTS

This work was authored by the National Renewable Energy Laboratory (NREL), operated by Alliance for Sustainable Energy, LLC, for the U.S. Department of Energy (DOE) under Contract No. DE-AC36-08GO28308. This work was supported by the Laboratory Directed Research and Development (LDRD) Program at NREL. Funding supporting development and operation of synthesis and characterization equipment was provided by the DOE Office of Science, Office of Basic Energy Sciences. Funding supporting GW calculations was provided by the DOE Office of Science collaboratively from the Office of Basic Energy Sciences, Division of Materials Science and the Advanced Scientific Computing Research (ASCR) program. This work used computational resources sponsored by the Department of Energy's Office of Energy Efficiency and Renewable Energy, located at NREL. Magnetometry was supported by the National Science Foundation through DMR-1905909. This research used resources of the Advanced Photon Source, a U.S. Department of Energy (DOE) Office of Science user facility operated for the DOE Office of Science by Argonne National Laboratory under Contract No. DE-AC02-06CH11357. The authors thank G.L. Brennecka for helpful discussions; R. Sherbondy for growing the $CeWN_{3-y}$ film; O.L. Borkiewicz for assistance at APS beamline 11-ID-B; and C.L. Rom for assistance with sample masking. The views expressed in the article do not necessarily represent the views of the DOE or the U.S. Government.

R.W.S., K.R.T., and A.Z. conceptualized the work; R.W.S. performed thin film growth and characterization (XRD, XRF), with assistance and input from J.S.M. (ellipsometry), I.L. (resistivity and magnetoresistance), M.H. (UV-vis), and J.C. and C.P.M. (photoresistivity). C.L.P. performed the AES measurements and analysis. S.E. provided access to the MPMS3. S.R.B. and A.Z. advised project directions. R.W.S. wrote the manuscript with input from all authors.

[1] V. M. Goldschmidt, Die Gesetze der Krystallochemie, Naturwissenschaften **14**, 477 (1926).

[2] H. D. Megaw, Crystal structure of barium titanate, Nature (London) **155**, 484 (1945).

[3] W. Sun, C. J. Bartel, E. Arca, S. R. Bauers, B. Matthews, B. Orvañanos, B. R. Chen, M. F. Toney, L. T. Schelhas, W. Tumas *et al.*, A map of the inorganic ternary metal nitrides, Nat. Mater. **18**, 732 (2019).

[4] A. Zakutayev, S. R. Bauers, and S. Lany, Experimental synthesis of theoretically predicted multivalent ternary nitride materials, Chem. Mater. **34**, 1418 (2022).

[5] R. Niewa, Metal-Rich Ternary perovskite nitrides, Eur. J. Inorg. Chem. **2019**, 3647 (2019).

[6] N. E. Brese and F. DiSalvo, Synthesis of the first thorium-containing nitride perovskite, $TaThN_3$, J. Solid State Chem. **120**, 378 (1995).

[7] V. V. Bannikov, I. R. Shein, and A. L. Ivanovskii, Electronic structure, chemical bonding and elastic properties of the first thorium-containing nitride perovskite $TaThN_3$, Phys. Stat. Sol. (RRL) **1**, 89 (2007).

[8] M.-C. Jung, K.-W. Lee, and W. E. Pickett, Perovskite $ThTaN_3$: A large-thermopower topological crystalline insulator, Phys. Rev. B **97**, 121104(R) (2018).

[9] P. Bacher, P. Antoine, R. Marchand, P. L'Haridon, Y. Laurent, and G. Roult, Time-of-flight neutron diffraction study of the structure of the perovskite-type oxynitride $LaWO_{0.6}N_{2.4}$, J. Solid State Chem. **77**, 67 (1988).

[10] S. J. Clarke, B. P. Guinot, C. W. Michie, M. J. Calmont, and M. J. Rosseinsky, Oxynitride perovskites: Synthesis and structures of $LaZrO_2N$, $NdTiO_2N$, and $LaTiO_2N$ and comparison with oxide perovskites, Chem. Mater. **14**, 288 (2002).

[11] M. Yang, J. Oró-Solé, A. Kusmartseva, A. Fuertes, and J. P. Attfield, Electronic tuning of two metals and colossal magnetoresistances in $EuWO_{1+x}N_{2-x}$ perovskites, J. Am. Chem. Soc. **132**, 4822 (2010).

[12] A. Fuertes, Chemistry and applications of oxynitride perovskites, J. Mater. Chem. **22**, 3293 (2012).

[13] A. P. Black, H. E. Johnston, J. Oro, C. Ritter, C. Frontera, J. P. Attfield, and A. Fuertes, Nitride tuning of lanthanide chromites, Chem. Commun. **52**, 4317 (2016).

[14] K. R. Talley, J. Mangum, C. L. Perkins, R. Woods-Robinson, A. Mehta, B. P. Gorman, G. L. Brennecka, and A. Zakutayev, Synthesis of lanthanum tungsten oxynitride perovskite thin films, Adv. Electron. Mater. **5**, 1900214 (2019).

[15] R. Sarmiento-Pérez, T. F. T. Cerqueira, S. Körbel, S. Botti, and M. A. L. Marques, Prediction of stable nitride perovskites, Chem. Mater. **27**, 5957 (2015).

[16] S. Körbel, M. A. Marques, and S. Botti, Stability and electronic properties of new inorganic perovskites from high-throughput: *Ab initio* calculations, J. Mater. Chem. C **4**, 3157 (2016).

[17] J. A. Flores-Livas, R. Sarmiento-Pérez, S. Botti, S. Goedecker, and M. A. L. Marques, Rare-earth magnetic nitride perovskites, J. Phys.: Mater. **2**, 025003 (2019).

[18] B. F. Grosso, D. W. Davies, B. Zhu, A. Walsh, and D. O. Scanlon, Accessible chemical space for metal nitride perovskites, Chem. Sci. (2023), doi: 10.1039/D3SC02171H.

[19] Y.-W. Fang, C. A. J. Fisher, A. Kuwabara, X.-W. Shen, T. Ogawa, H. Moriwake, R. Huang, and C.-G. Duan, Lattice dynamics and ferroelectric properties of the nitride perovskite $LaWN_3$, Phys. Rev. B **95**, 014111 (2017).

[20] S. Singh and M. N. Tripathi, Sr-doped $LaMoN_3$ and $LaWN_3$: New degenerate p-type nitrides, J. Appl. Phys. **124**, 065109 (2018).

[21] S. Bandyopadhyay, A. Paul, and I. Dasgupta, Origin of Rashba-Dresselhaus effect in the ferroelectric nitride perovskite $LaWN_3$, Phys. Rev. B **101**, 014109 (2020).

[22] X. Liu, J. Fu, and G. Chen, First-principles calculations of electronic structure and optical and elastic properties of the novel ABX_3-type $LaWN_3$ perovskite structure, RSC Advances **10**, 17317 (2020).

[23] S. Matsuishi, D. Iwasaki, and H. Hosono, Synthesis of perovskite-type $LaWN_3$ by high-pressure solid-state metathesis reaction, J. Solid State Chem. **315**, 123508 (2022).

[24] S. Geng and Z. Xiao, Can nitride perovskites provide the same superior optoelectronic properties as lead halide perovskites? ACS Energy Lett. **8**, 2051 (2023).

[25] K. R. Talley, C. L. Perkins, D. R. Diercks, G. L. Brennecka, and A. Zakutayev, Synthesis of $LaWN_3$ nitride perovskite with polar symmetry, Science **374**, 1488 (2021).

[26] R. Sherbondy, R. W. Smaha, C. J. Bartel, M. E. Holtz, K. R. Talley, B. Levy-Wendt, C. L. Perkins, S. Eley, A. Zakutayev, and G. L. Brennecka, High-throughput selection and experimental realization of two Nnew Ce-based nitride perovskites: $CeMoN_3$ and $CeWN_3$, Chem. Mater. **34**, 6883 (2022).

[27] S. D. Kloß, M. L. Weidemann, and J. P. Attfield, Preparation of bulk-phase nitride Pperovskite $LaReN_3$ and topotactic reduction to $LaNiO_2$-type $LaReN_2$, Angew. Chem. Int. Ed. **60**, 22260 (2021).

[28] K. R. Talley, S. R. Bauers, C. L. Melamed, M. C. Papac, K. N. Heinselman, I. Khan, D. M. Roberts, V. Jacobson, A. Mis, G. L. Brennecka *et al.*, COMBIgor: Data-analysis package for combinatorial materials science, ACS Comb. Sci. **21**, 537 (2019).

[29] https://htem.nrel.gov.

[30] A. Zakutayev, N. Wunder, M. Schwarting, J. D. Perkins, R. White, K. Munch, W. Tumas, and C. Phillips, An open experimental database for exploring inorganic materials, Sci. Data **5**, 180053 (2018).

[31] *Handbook of Auger Electron Spectroscopy: A Book of Reference Data for Identification and Interpretation in Auger Electron Spectroscopy*, 3rd ed, edited by K. D. Childs and C. L. Hedberg (Physical Electronics, Eden Prairie, 1995).

[32] B. H. Toby and R. B. Von Dreele, *GSAS-II*: The genesis of a modern open-source all purpose crystallography software package, J. Appl. Crystallogr. **46**, 544 (2013).

[33] Y. Liu, Q. X. Li, L. Y. Wan, B. Kucukgok, E. Ghafari, I. T. Ferguson, X. Zhang, S. Wang, Z. C. Feng, and N. Lu, Composition and temperature dependent optical properties of $Al_xGa_{1-x}N$ alloy by spectroscopic ellipsometry, Appl. Surf. Sci. **421**, 389 (2017).

[34] G. Kresse and J. Furthmüller, Efficiency of *ab-initio* total energy calculations for metals and semiconductors using a plane-wave basis set, Comput. Mater. Sci. **6**, 15 (1996).

[35] G. Kresse and J. Furthmüller, Efficient iterative schemes for *ab initio* total-energy calculations using a plane-wave basis set, Phys. Rev. B **54**, 11169 (1996).

[36] G. Kresse and D. Joubert, From ultrasoft pseudopotentials to the projector augmented-wave method, Phys. Rev. B **59**, 1758 (1999).

[37] P. Gorai, E. S. Toberer, and V. Stevanović, Thermoelectricity in transition metal compounds: The role of spin disorder, Phys. Chem. Chem. Phys. **18**, 31777 (2016).

[38] V. Stevanović, S. Lany, X. Zhang, and A. Zunger, Correcting density functional theory for accurate predictions of compound

enthalpies of formation: Fitted elemental-phase reference energies, Phys. Rev. B **85**, 115104 (2012).

[39] J. Qu, V. Stevanović, E. Ertekin, and P. Gorai, Doping by design: finding new n-type dopable ABX_4 Zintl phases for thermoelectrics, J. Mater. Chem. A **8**, 25306 (2020).

[40] P. Gorai, T. Famprikis, B. Singh, V. Stevanovic, and P. Canepa, Devil is in the defects: electronic conductivity in solid electrolytes, Chem. Mater. **33**, 7484 (2021).

[41] See Supplemental Material at http://link.aps.org/supplemental/10.1103/PhysRevMaterials.7.084411 for additional AES data, SEM data, additional XRD data, additional transport data, and additional magnetism data.

[42] M. J. Brett and R. R. Parsons, Stoichiometry control mechanisms for bias-sputtered zinc-oxide thin films, Can. J. Phys. **63**, 819 (1985).

[43] R. Castellano, M. Notis, and G. Simmons, Composition and stress state of thin films deposited by ion beam sputtering, Vacuum **27**, 109 (1977).

[44] Y. Igasaki and H. Mitsuhashi, The effects of substrate bias on the structural and electrical properties of TiN films prepared by reactive r.f. sputtering, Thin Solid Films **70**, 17 (1980).

[45] Z. Kabilova, C. Kurdak, and R. L. Peterson, Observation of impurity band conduction and variable range hopping in heavily doped (010) β-Ga2O3, Semicond. Sci. Technol. **34**, 03LT02 (2019).

[46] T. H. Culman, R. Woods-Robinson, J. S. Mangum, R. W. Smaha, C. L. Rom, A. Zakutayev, and S. R. Bauers, Nitrogen stabilizes the wurtzite polymorph in $ZnSe_{1-x}Te_x$ thin films, J. Mater. Chem. C **10**, 15806 (2022).

[47] M. M. Parish and P. B. Littlewood, Non-saturating magnetoresistance in heavily disordered semiconductors, Nature (London) **426**, 162 (2003).

[48] J. Hu and T. F. Rosenbaum, Classical and quantum routes to linear magnetoresistance, Nat. Mater. **7**, 697 (2008).

[49] J. C. W. Song, G. Refael, and P. A. Lee, Linear magnetoresistance in metals: Guiding center diffusion in a smooth random potential, Phys. Rev. B **92**, 180204(R) (2015).

[50] F. Kisslinger, C. Ott, and H. B. Weber, Origin of nonsaturating linear magnetoresistivity, Phys. Rev. B **95**, 024204 (2017).

[51] S. R. Bauers, A. Holder, W. Sun, C. L. Melamed, R. Woods-Robinson, J. Mangum, J. Perkins, W. Tumas, B. Gorman, A. Tamboli *et al.*, Ternary nitride semiconductors in the rock-salt crystal structure, Proc. Natl. Acad. Sci. USA **116**, 14829 (2019).

[52] C. L. Rom, R. W. Smaha, C. L. Melamed, R. R. Schnepf, K. N. Heinselman, J. S. Mangum, S.-J. Lee, S. Lany, L. T. Schelhas, A. L. Greenaway *et al.*, Combinatorial synthesis of cation-disordered manganese tin nitride $MnSnN_2$ thin films with magnetic and semiconducting properties, Chem. Mater. **35**, 2936 (2023).

[53] S. R. Bauers, J. Mangum, S. P. Harvey, J. D. Perkins, B. Gorman, and A. Zakutayev, Epitaxial growth of rock salt $MgZrN_2$ semiconductors on MgO and GaN, Appl. Phys. Lett. **116**, 102102 (2020).